Advanced Synthesis & Catalysis

ADVANCED SYNTHESIS & CATALYSIS
advsynthcatal.com

RESEARCH ARTICLE OPEN ACCESS

Structural Features and Reaction Profile of an Evolved Unspecific Peroxygenase From *Candolleomyces Aberdarensis*

Andrea Menés-Rubio[1] | Angela Fernandez-Garcia[2,3] | Miquel A. Galmes-Ordinas[1] | Patricia Gomez de Santos[4] | Israel Sanchez-Moreno[1,5] | Julia Sanz-Aparicio[2] | Miguel Alcalde[1]

[1]Department of Biocatalysis, Institute of Catalysis-CSIC, Madrid, Spain | [2]Department Crystallography & Structural Biology, Instituto de Química Física Blas Cabrera (IQF), Madrid, Spain | [3]Institute of Phototrophic Microbiology, Heinrich Heine University, Düsseldorf, Germany | [4]EvoEnzyme S.L., Parque Científico de Madrid, Madrid, Spain | [5]Department of Bio-Organic Chemistry, Instituto de Química Orgánica General (IQOG), Madrid, Spain

Correspondence: Miguel Alcalde (malcalde@icp.csic.es)

Received: 31 October 2025 | **Revised:** 27 February 2026 | **Accepted:** 25 March 2026

Keywords: alkanes | C–H oxyfunctionalizations | crystal structure | fatty acids | molecular dynamics | norisoprenoids | unspecific peroxygenase

ABSTRACT

Fungal unspecific peroxygenases (UPOs) are versatile biocatalysts capable of inserting oxygen into nonactivated C—H bonds. Despite their significance in organic synthesis, only a few UPOs have been characterized structurally and biochemically. In the current study, we provide insights into the structure and reaction profile of an unusual, acidic, long UPO from *Candolleomyces aberdarensis* that was evolved for heterologous expression in yeast. The crystal structure of the enzyme was resolved at a resolution of 1.8 Å, which helped to reveal several catalytic determinants that differ from those of canonical long UPOs. Cocrystallization experiments with alkanes, fatty acids, and the norisoprenoids α-damascone and α-ionone, were carried out together with the analysis of enzymatic reactions. With alkanes and fatty acids, the biocatalyst performs oxygenations at the $\omega-1$ and $\omega-2$ positions, producing diols and ketones. Conversely, the enzyme acts on the α-ionone ring and the vinylic aliphatic chain of α-damascone, generating 3-hydroxy-α-ionone and 10-hydroxy-α-damascone, respectively. The substrate preferences of this biocatalyst are marked by an intensely hydrophobic heme channel, with some residues protruding into the tunnel, and a characteristic catalytic tripod comprising a Met residue in a dual conformation. Molecular dynamics simulations revealed that enzyme catalysis is primarily driven by dynamic channel gating, ligand-specific preorganization within the access tunnel, and complex diffusion pathways leading to the active site.

1 | Introduction

Following their discovery more than two decades ago, the heme-thiolate containing unspecific peroxygenase (UPO, EC 1.11.2.1) has steadily gained recognition as versatile biocatalyst for organic synthesis. UPO naturally inserts oxygen into inert C—H bonds of both aliphatic and aromatic compounds, and the beauty of this fungal enzyme stems from its simplicity. It is extracellular, soluble, and it performs the most demanding oxyfunctionalization reactions relying solely on hydrogen peroxide as the final electron acceptor and the main oxygen donor [1–3]. Beyond standard organic chemistry, UPO offers a springboard to achieve more complex biotransformations, for example, through new-to-nature chemistry, as reflected recently in the synthesis of organosilanes, and in anti-Markovnikov oxidation, cyclopropanation, or nitrene insertion reactions [4–8].

UPOs are sorted into two phylogenetic groups: Family I (short UPOs), which includes homodimers made up of ≈26 kDa monomers with histidine as a charge stabilizer; and Family II

Andrea Menés-Rubio and Angela Fernandez-Garcia contributed equally to this work.

(long UPOs), that are ≈44 kDa monomeric enzymes with arginine as a charge stabilizer. Both long and short UPOs differ in their structural features, with the geometry of the heme channel dictating their substrate profile and product selectivity [1–3]. Despite the growing interest in these enzymes, to date only seven UPOs have been fully characterized at the structural and biochemical level, of which only two are long UPOs [3, 9–12]. Consequently, the key representative of the long UPOs is the prototypic *Cyclocybe* (*Agrocybe*) *aegerita* UPO (*Aae*UPO), together with its PaDa-I mutant that was engineered by directed evolution for secretion in yeast, both of which have been the subject of a large number of studies in the field [1–3, 13–15]. More recently, two unusual acidic peroxygenases from the African ink cap *Candolleomyces* (*Psathyrella*) *aberdarensis* were subjected to engineering, *Pab*UPO-I and *Pab*UPO-II [16]. Like PaDa-I, these long UPOs were designed to be readily secreted by both *Saccharomyces cerevisiae* and *Pichia pastoris* (*Komagataella phaffii*). A recent crystallographic characterization of *Pab*UPO-II was also coupled to an analysis of substrate selectivity [17]. To complement this work, we now present the crystallographic and substrate analysis of the Grogu variant derived from *Pab*UPO-I, which was engineered by attaching the evolved signal peptide from PaDa-I to *Pab*UPO-I and by inserting a mutational backbone for secretion (S61A-L79I-A252L), also from PaDa-I. The Grogu mutant is readily expressed by *S. cerevisiae* (14 mg/L) and it can be produced in *P. pastoris* in a fed-batch bioreactor at 240 mg/L without any optimization of the process. This UPO is both very active and stable, and it maintains its peroxygenase activity over an unusually broad pH range, from pH 3–9 (retaining over 80% activity from pH 4–8). This latter characteristic may be an attractive feature in future industrial applications with enzyme cascade reactions [16].

In the current study, the Grogu mutant was crystallized at high resolution, obtaining complexes with model substrates (alkanes, fatty acids, and norisoprenoids), assessing its profile of selectivity toward these compounds in enzymatic reactions analyzed by gas chromatography/mass spectrometry (GC/MS). Molecular dynamics (MD) simulations helped to shed light on the catalytic performance of this enzyme.

2 | Results and Discussion

2.1 | Structural Features of the Grogu Mutant

The Grogu variant was produced by *P. pastoris* in a 5L fed-batch bioreactor and purified to homogeneity (Reinheitszahl value [Rz] $A_{418}/A_{280} = 2$). The recombinant enzyme had a MW of 43,000 Da, to which glycosylation contributes 14%. Attempts to crystallize a deglycosylated form (*i.e.*, after enzymatic reaction with Endo H) were unfruitful, such that the successive experiments were performed on the glycosylated enzyme. High-quality large plate crystals of the Grogu variant were grown in a solution of 6–16% polyethylene glycol (PEG) 8000, 0.1 M 4-(2-sulfonatoethyl)morpholin-4-ium (MES) pH 6.5 and 0.15 M zinc chloride, providing diffraction data to 1.8 Å maximum resolution. These crystals belong to the $P6_5$ space group, with two molecules per asymmetric unit (see the **Material and Methods section** and the **Supplementary Table S1** for the full experimental details and procedures for structural determination).

The electron density maps allowed the whole polypeptide chain to be modeled, from Leu1 to Leu334. This model also contains one heme group, one structural Mg^{2+}, and three glycans at Asn16, Asn145, and Asn165 N-glycosylation sites. The glycan chains included *N*-acetyl-d-glucosamine (NAG), *β*-d-mannose (BMA), and *α*-d-mannose (MAN) units. Furthermore, some MES molecules from the crystallization buffer and glycerol molecules from the cryoprotectant were also bound to different positions at the surface of the molecule. According to the PDBePISA server, the asymmetric unit consists of two independent polypeptide chains [18], such that the functional enzyme is a monomer, as expected for a long UPO. These two molecules are essentially identical (root-mean-square deviation between chains of 0.2068 Å), the main differences being observed in the glycan chain attached to each polypeptide.

The ligand-free Grogu adopted a similar folding arrangement to the other two long UPOs crystallized to date –*Aae*UPO and *Pab*UPO-II [9, 10, 17]. Grogu, *Pab*UPO-II, and *Aae*UPO share ≈65% sequence identity, with an overall structure comprised of 10 *α*-helices and two short *β*-strands linked by long loops, Figure 1. The prosthetic heme group is surrounded by these loops and linked to Cys40, which is the proximal/axial ligand that constitutes the PCP motif (Pro39-Cys40-Pro41) described in UPOs [19]. The sixth coordination of the heme group is occupied by a water molecule acting as the distal ligand. Another common feature of long UPOs is an intramolecular disulfide bridge in the C-terminal domain, in this case between Cys285 and Cys325. As described for *Pab*UPO-II and *Aae*UPO [17], Grogu also has a structural magnesium ion (Mg^{2+}, represented as a green sphere in Figure 1), while the acid–base pair required for H_2O_2 cleavage is constituted by Arg193 and Glu200, the former acting as the enzyme's charge stabilizer, Figure 2.

The heme access channel forms a tunnel deep in the molecule that displays notable differences from that of the other long UPOs. First, phenylalanine residues (Phe80 and Phe195) at the channel entrance define the upper region of the tunnel in

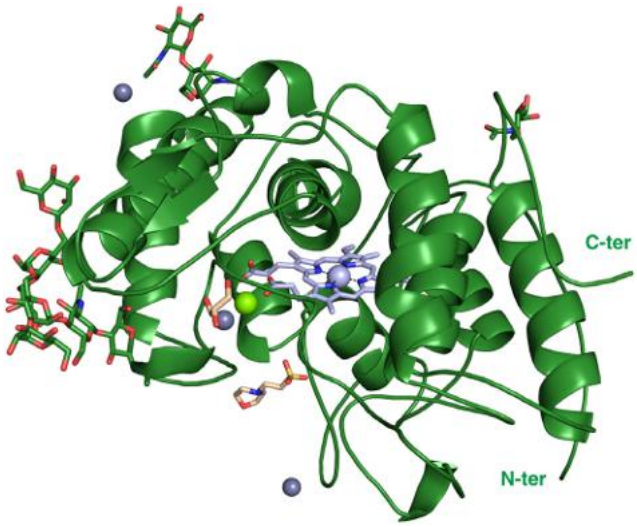

FIGURE 1 | Overall folding of the Grogu variant. The heme group (in light violet), glycan chains (in green), and the glycerol and MES molecules (in beige) are shown in sticks. The magnesium cation (Mg^{2+}) is represented by a light green sphere and several zinc cations (Zn^{2+}) captured in the crystal are represented by violet spheres.

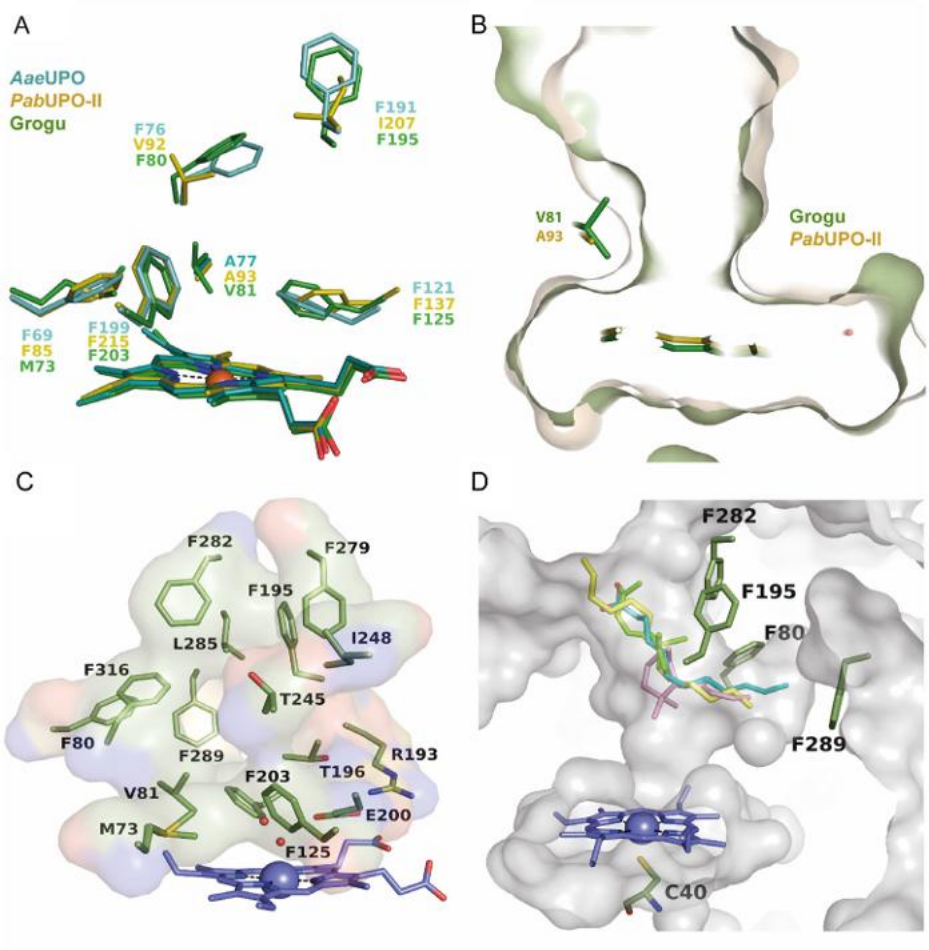

FIGURE 2 | The heme access channel of Grogu. (A) The main structural features of Grogu depicted as green sticks and compared to *Aae*UPO and *Pab*UPO-II, whose residues are represented as blue and orange sticks, respectively. The colored labels correspond to each enzyme. (B) Structural differences between the surfaces of Grogu (green) and *Pab*UPO-II (beige). (C) Residues defining the heme channel of Grogu presented as green sticks and water molecules depicted by red spheres. (D) The Grogu heme channel shown with ligands bound in the complexes. The heme group is represented by violet sticks, with axial ligand Cys40 and relevant phenylalanines shaping the channel (Phe80, 195, 282, and 289) depicted by green sticks.

the Grogu mutant, similar to Phe76 and Phe191 in *Aae*UPO, Figure 2A. A key difference relative to *Aae*UPO is that these aromatic residues are found in a unique conformation in Grogu and, therefore, the flexibility described in *Aae*UPO that was considered essential in the substrate trafficking to the active site of this enzyme [9, 10] was not evidenced in Grogu. Conversely, two aliphatic amino acids reside at equivalent positions in *Pab*UPO-II (Val92 and Ile207). Regarding the aromatic triad involved in positioning the substrate close to the heme, this is almost identical in both *Pab*UPO-II (Phe85, Phe137, and Phe215) and *Aae*UPO (Phe69, Phe121, and Phe199) [17], whereas one of these phenylalanines is substituted by a methionine residue in the Grogu variant (Met73), completing the triad with Phe125 and Phe203 in a similar fashion to the long UPO from *Coprinopsis cinerea* [20]. This methionine presents a dual conformation in some of the complexes, which could possibly be involved in a dynamic trafficking of substrates during catalysis, Figure 2A,C.

Indeed, analysis of MD trajectories (Figure 3) showed a strong correlation between the dual conformation of Met73 and the geometry of the heme access channel. Principal component analysis of channel shape descriptors indicates that Met73 conformations A and B populate distinct regions on the projected conformational space, corresponding to different degrees of channel access openness (Figure 3A). Representative structures extracted from these conformational basins reveal that changes in the channel shape are associated with a progressive widening and opening of the channel cavity, which supports the role of the Met73 as a dynamic gating mechanism regulating substrate trafficking (Figure 3B,C).

The active site of Grogu is also shaped by Val81 that protrudes into the middle of the channel, which may hinder the entry of bulky substrates, Figure 2B. In addition, Glu200 contributes to the acid–base pair and it appears to partially cover the heme group, while apparently obstructing the approach to heme, Figure 2C. Overall, the channel is highly hydrophobic, containing only a few polar residues (*e.g.*, Thr196 and Thr245). Notably, it is enriched in phenylalanine residues (Phe80, Phe195, Phe279, Phe282, Phe289, and Phe316). Among these, Phe80, Phe195, and Phe289 delineate a singular pocket that plays a key role in substrate binding at a position distal to the heme, Figure 2C,D. As shown in the structural alignment of *Aae*UPO, *Pab*UPO-II, and the Grogu variant (**Supplementary Figure S1)**, only Phe279 is conserved in the *Pab*UPO-II sequence (corresponding to Phe292), whose heme channel contains only one additional

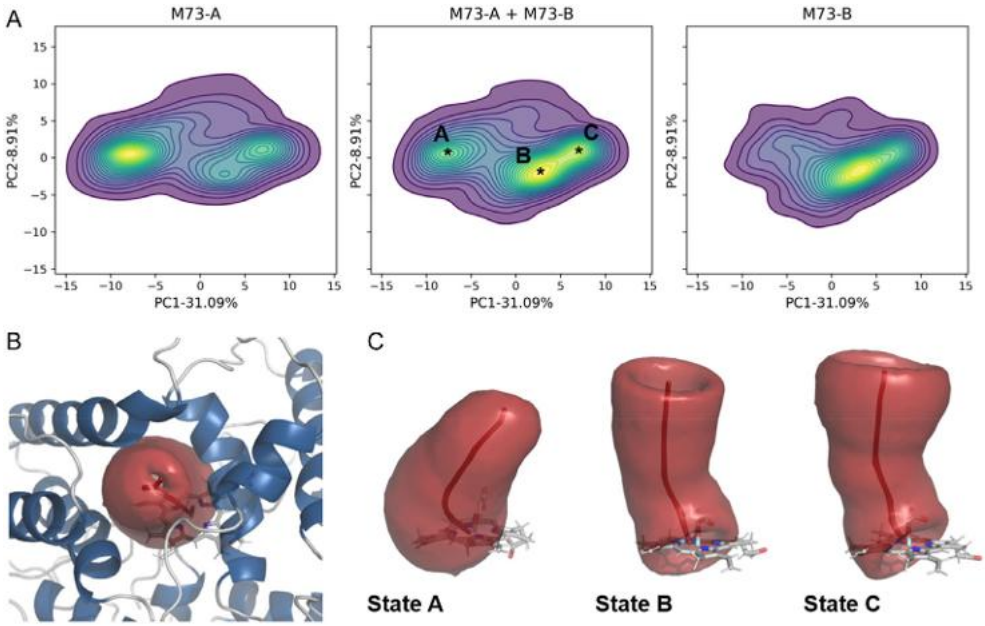

FIGURE 3 | Conformational states of Grogu channel. (A) Kernel density estimates computed from the PCA of channel descriptors along the MD trajectories. Projections are shown for Met73 in conformation A (left), pooled Met73 A and B (center), and Met73 in conformation B (right). In the combined dataset, three dominant basins corresponding to States A, B, and C are highlighted, representing distinct channel conformations. (B) Representative structure depicting the location of the channel shape and centerline (in red) relative to Grogu structure. (C) Representative channel geometries corresponding to States A, B, and C extracted from the PCA maxima. MD = Molecular dynamics; PCA = principal component analysis.

phenylalanine residue (Phe336) [21]. This alignment also highlights that the residues shaping the heme channel are predominantly located within regions of regular secondary structures, namely helices α3, α6, and α9, (**Supplementary Figure S1**). In Grogu, the phenylalanine residues Phe80 (helix α3), Phe195 (helix α6), and Phe289 (helix α9), which define the distinctive lateral enlargement of the heme channel described above, are all positioned within these helices. Although these three phenylalanines are conserved in the *Aae*UPO sequence, a comparable pocket is not formed within its heme channel, mainly due to two key differences. First, the presence of Phe188 in helix α6 of *Aae*UPO (corresponding to Pro192 in the Grogu variant) sterically occludes the pocket observed in Grogu, Figure 4. Second, the position occupied by Phe282 in helix α9 of Grogu is replaced by Pro277 in *Aae*UPO. Collectively, these subtle variations give rise to a distinct overall channel geometry and, consequently, account for the pronounced differences observed in ligand binding modes among these peroxygenases.

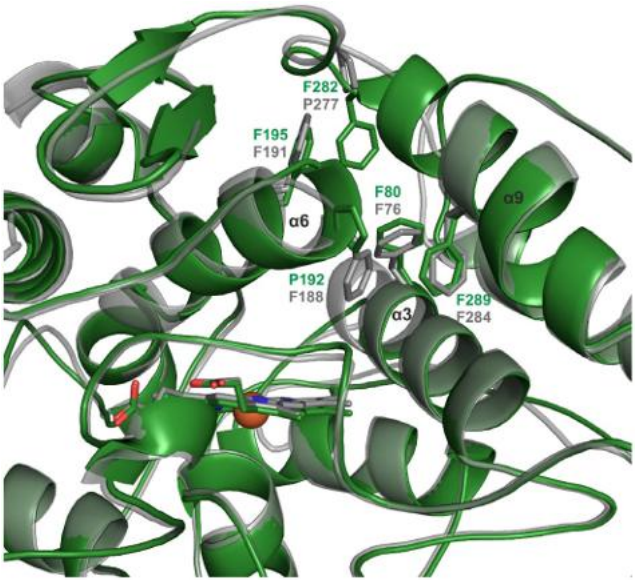

FIGURE 4 | Comparison of Grogu variant, in green, and *Aae*UPO (PDB code: 2YOR), in gray. The relevant residues located in helices α3, α6, and α9 are represented with sticks, as well as the heme group of each peroxygenase.

2.2 | Cocrystallization and Enzymatic Studies

Grogu crystals were examined in soaking and cocrystallization experiments with model substrates tetradecane, lauric acid, and norisoprenoids (α-damascone and α-ionone), but only cocrystallization strategy led to the complexes shown in Figure 2D and Figure 5 (see the **Materials and Methods section** and **Supplementary Table S1** for the full crystallographic details of these complexes). The electron density evident in the heme channel reflected ligand binding in all the complexes, albeit far from the heme and consequently, in an apparently noncatalytic position. The heme channel has several water molecules in the upper zone, as well as two water molecules directly coordinated to the iron heme, mimicking Compound I described in the reaction mechanism of UPOs. All these ligands seem to be stabilized in the hydrophobic cavity formed by the aromatic residues in the middle of the channel where an enlargement is observed, Figure 2D and Figure 5.

The complexes with tetradecane and lauric acid suggested a precatalytic state in an extended conformation, which may be stabilized by hydrophobic interactions with Ile248, Phe279, and Phe282

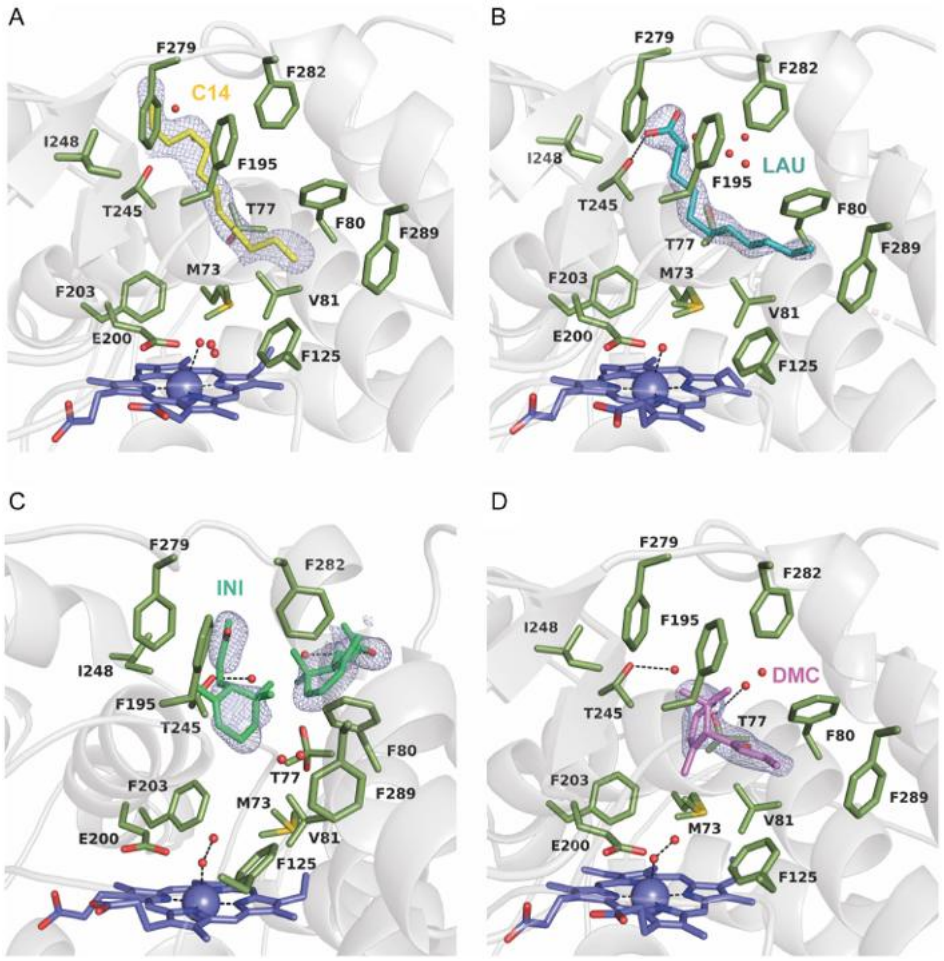

FIGURE 5 | The crystal structures of Grogu complexed with substrates: (A) tetradecane (C14), (B) lauric acid (LAU), (C) α-ionone (INI), (D) α-damascone (DMC). The residues defining the heme channel are represented as green sticks and the polar bonds are shown as dashed lines. Water molecules involved in substrate recognition are included as red spheres and the $2F_0$–Fc electron density at the ligands has been contoured at 0.8–1.0 σ.

at the entrance of the channel. In addition, the other end of the aliphatic chain is packed between Phe80, Phe195, and Phe289. The regioselectivity of Grogu was analyzed by GC/MS with the alkanes (tetradecane and dodecane) and fatty acids (myristic and lauric acid), noting subterminal hydroxylation at ω−1 and ω−2 in all cases. With tetradecane (C14) and dodecane (C12), Grogu behaved like *Pab*UPO-II and *Aae*UPO [17, 20], achieving full conversion to generate diols as well as ketones, the latter the result of overoxidation reactions, Figure 6A,B, **Supplementary Table S2**. With fatty acids, only ω−1 and ω−2 subterminal alcohols were detected, with no further overoxidation products due to the lower conversion yields, Figure 6C,D, **Supplementary Table S2**. In addition to subterminal oxidations of fatty acids, *Pab*UPO-II previously showed α- and β-hydroxylation on diacids, a potential carbon chain-shortening reaction of particular interest [17]. However, Grogu was not active in reactions with dodecanedioic and tetradecanedioic acids (data not shown).

Norisoprenoids, such as α-ionone and α-damascone, were captured in the crystal at the entrance of the active site channel, stabilized by hydrophobic interactions with the aromatic residues of the channel, Figure 5C,D. For α-ionone, two molecules were found in the tunnel with their ring pointing to the heme, their carbonyl group establishing polar bonds with water molecules in the upper zone, Figure 5C. GC/MS analyses showed that the enzyme attacks α-ionone's ring at C3, generating 3-hydroxy-α-ionone (3-OH-α-I) as reported for *Pab*UPO-II and *Aae*UPO, Figure 7A, **Supplementary Table S2** [17, 22]. In terms of α-damascone, the crystallographic complex showed the ligand oriented opposite to that of α-ionone, that is, parallel to the heme and with its keto-alkenyl group directed toward the tunnel enlargement, Figure 5D. When the enzymatic reaction with α-damascone and Grogu was assessed, only the attack of the allylic carbon was witnessed, specifically at the C10 position, generating 10-hydroxy-α-damascone (10-OH-α-D), Figure 7B, **Supplementary Table S2**. Grogu also performed stepwise oxidations producing the corresponding carboxylated product (10-COOH-α-D), as also happens with *Aae*UPO and *Pab*UPO-II [17, 22]. Unlike *Pab*UPO-II, we did not detect the formation of 3-hydroxy-α-damascone, a consequence of attacking the C3 of the ring, indicating that the regioselectivity of Grogu is exclusively focused on the vinylic aliphatic chain.

The computational analysis of the substrate access channel provides a framework for these findings. MD simulations revealed that access to the catalytic cavity is gated by the opening of the distal region of the channel. Docking studies of α-ionone and α-damascone, performed on representative channel conformations (States A, B, and C, Figure 3), show that channel opening is required for substrates to adopt reactive geometries within the active site cavity, **Supplementary Figure S2**. This substrate access modulation is in agreement with the precatalytic

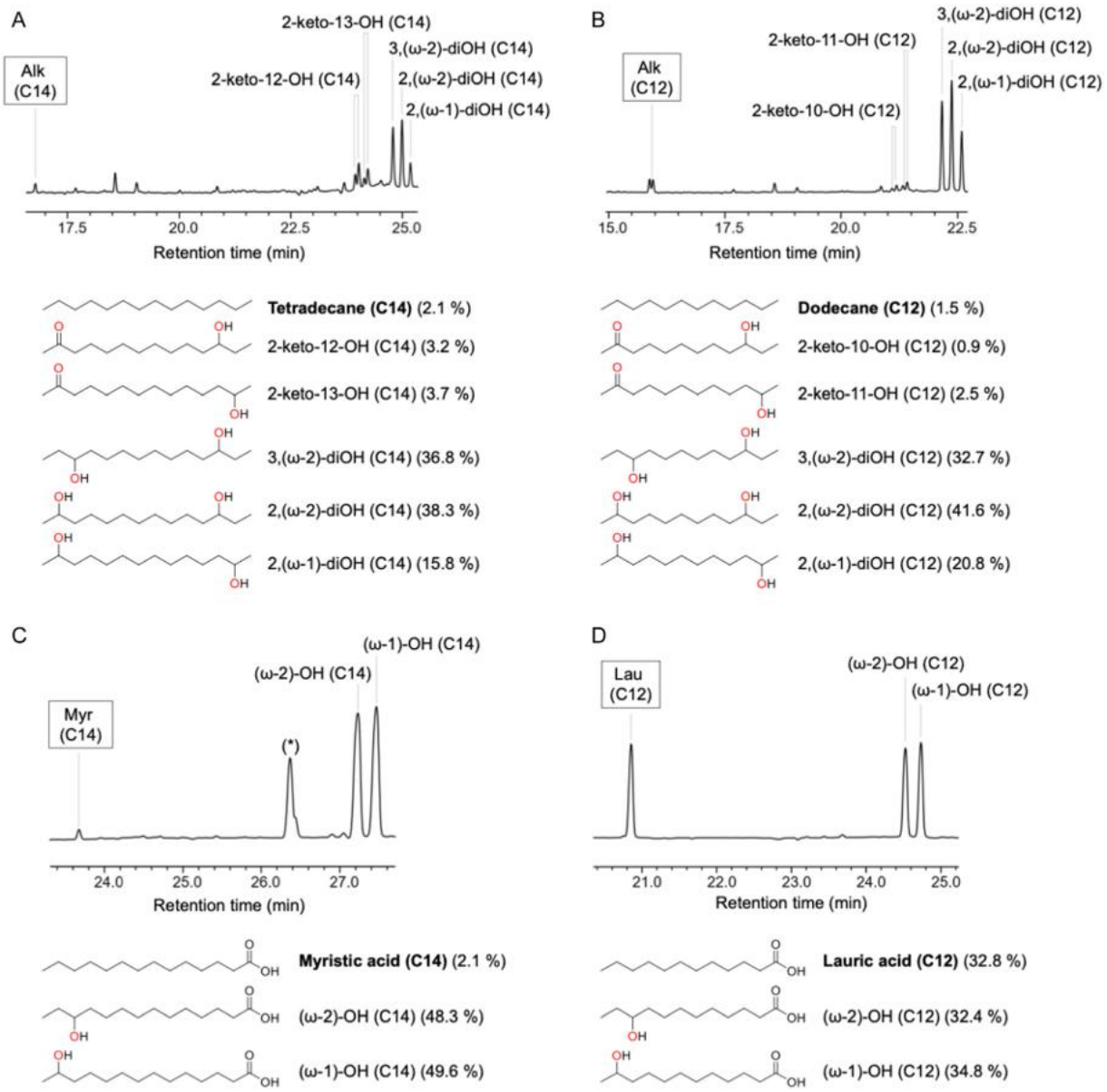

FIGURE 6 | GC/MS analyses of Grogu reactions with (A) tetradecane (C14), (B) dodecane (C12), (C) myristic acid (Myr), and (D) lauric acid (Lau). Reactions contained 0.3 mM of alkanes or 0.1 mM of the fatty acids as substrates, 50 mM potassium phosphate buffer pH 6.0, 2.5 mM H_2O_2, 1 μM of the pure enzyme, and acetone 20% (*v*/*v*), in a final reaction volume of 2.5 mL. The reactions were incubated for 1 h at 37°C (for alkanes) or for 2 h at 30°C (for fatty acids), with shaking at 210 rpm. The peaks marked with an (*) correspond to traces also present in the corresponding control for each reaction. GC/MS = Gas chromatography/mass spectrometry.

conformations observed in crystallographic structures. In this context, distances between potentially reactive carbons (C3 and C10 in α-ionone and α-damascone, respectively) and oxo-ferryl Cpd I were used as a proxy for assessing the state-dependent active site accessibility rather than the direct prediction of catalytically productive modes, **Supplementary Figure S2**. Additionally, MM/GBSA binding free energy calculations indicate that multiple poses are energetically accessible within open states, although do not fully explain the experimental observed regioselectivity. Altogether, these results suggest that regioselectivity in Grogu arises not only from differential binding, but from a combination of dynamic channel gating, ligand-specific preorganization within the access tunnel, and complex diffusion pathways toward the active site, which collectively increase the probability of forming catalytically productive geometries.

In sum, the orientation of the substrates observed in the complexes described here aligns with the selectivity experimentally determined for Grogu. Nevertheless, all substrates remain positioned at a certain distance from the heme, consistent with a pre-catalytic conformation. This observation supports the notion that the dynamic substrate trafficking previously proposed for this enzyme family may play a crucial role in achieving the final, catalytically competent positioning.

3 | Conclusions

This work provides structural information and functional insights into the *Pab*UPO-I Grogu mutant. This is the third long UPO crystallized to date, opening avenues for further

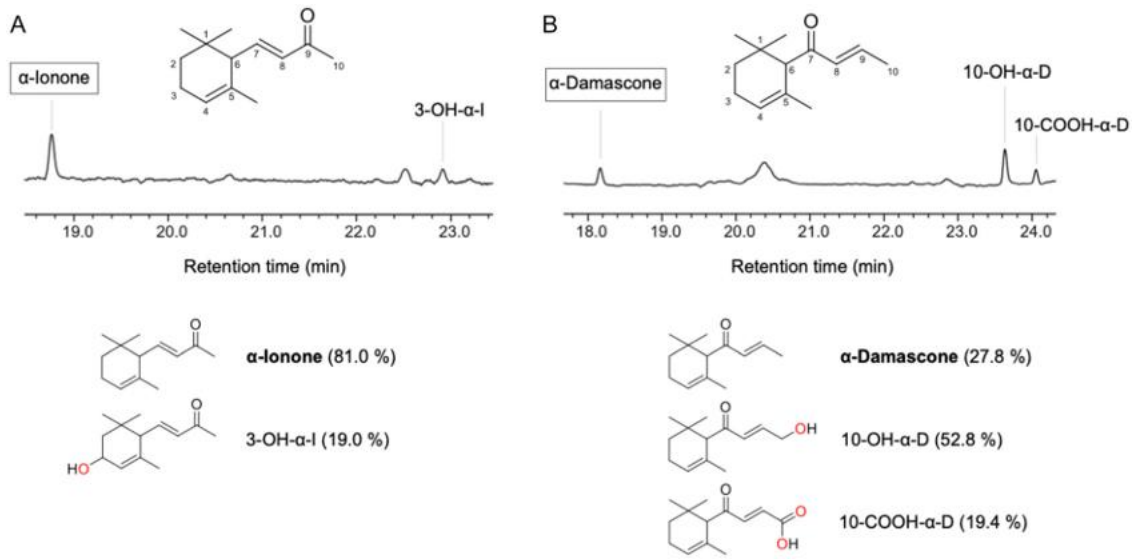

FIGURE 7 | GC/MS analyses of the reactions of Grogu with (A) α-ionone (INI) and (B) α-damascone (DMC). Reactions were performed with 0.5 mM of the substrates, in 50 mM potassium phosphate buffer pH 6.0, 2.5 mM H_2O_2, 0.5 μM of the pure enzyme, in a final reaction volume of 1 mL. The reactions were incubated for 30 min at 30°C, with shaking at 210 rpm. GC/MS = Gas chromatography/mass spectrometry.

structure-guided engineering studies. The highly dynamic substrate diffusion into the heme site is mainly driven by hydrophobic interactions, with several phenylalanines surrounding the lateral enlargement of the catalytic site. Crystallographic assays combined with GC/MS analyses indicate that Grogu can hydroxylate linear alkanes and fatty acids at subterminal positions, and it can also carry out overoxidation reactions to give rise to diols and ketones. With the norisoprenoids α-ionone and α-damascone, the biocatalyst displayed quite regioselective, targeting oxygenations to the ring or the aliphatic chain, respectively. The selectivity and specificity of this biocatalyst could be modulated in the near future by subjecting residues protruding into the tunnel, or those involved in the catalytic tripod, to machine-learning guided directed evolution or to FuncLib atomistic design (work in progress) [23]. Along these lines, the generation of chimeras enriched in sequence and function (using Grogu, *Pab*UPO-II, and *Aae*UPO as parental enzymes) will expand the portfolio of synthetic peroxygenases (work in progress) [24].

4 | Experimental Section

Chemicals: H_2O_2, *N*,O-Bis(trimethylsilyl)-trifluoroacetamide (BSTFA), and the substrates tetradecane, dodecane, myristic acid, lauric acid, α-ionone, α-damascone were purchased from Sigma-Aldrich (USA). Pyridine for derivatization was from Panreac AppliChem (ITW Reagents, USA). All chemicals and media components were of the highest purity available (at least ≥ 97%).

Production of Grogu in Pichia pastoris: Grogu variant was cloned, produced in a fed-batch bioreactor, and purified as described previously [17].

Crystallization and structure determination of Grogu and its complexes: For the screening of crystallization conditions, several commercial crystallization kits were tested using an Oryx8 robot (Douglas Instruments) in 96-well crystallization plates (Hampton Research). In particular, Index, SaltRx, and Crystal Screen I&II kits (Hampton Research) and JBS Classic, JBScreen JCSG++, and PACT packages (Jena Bioscience) were used. Crystals were grown by the sitting-drop vapor diffusion method at 18°C. After 3 weeks, the first crystals (in buffer 20 mM Tris-HCl pH 7.8) at a concentration of 17 mg/mL from the glycosylated form of Grogu were obtained in 2 M ammonium sulfate, 0.1 M Bis-Tris pH 6.5 or 0.1 M Tris-HCl pH 8.5. These crystals were hard to optimize and presented poor diffraction. Afterward, new screening conditions were tested so that crystals (in buffer K_2HPO_4 pH 7) at a concentration of 18 mg/mL grew in a different condition: 10% polyethylene glycol (PEG) 8000, 0.1 M MES pH 6.5, and 0.2 M zinc acetate. These crystals diffracted to a maximum resolution of 1.8 Å but contain an acetate anion, which is well known as an UPO inhibitor [10], bound to the active site. For that reason, zinc acetate was substituted for zinc chloride. The best plates were optimized in 6–16% PEG 8000, 0.1 M MES pH 6.5, and 0.15 M zinc chloride and protein/reservoir ratio of 1.5:1. For data collection, crystals were cryoprotected with 25% *v*/*v* glycerol previously to be immersed in liquid nitrogen.

Diffraction data were collected in XALOC beamline at ALBA synchrotron (Cerdanyola del Valles, Spain). Data were integrated and scaled with XDS [25] and then merged with AIMLESS program from the CCP4 package [26]. These crystals were indexed in the $P6_5$ space group, containing two molecules per asymmetric unit (mol/ASU) and 60% of solvent content within the unit cell. The structure of Grogu was solved by Molecular Replacement with MOLREP [27] using the coordinates of *Pab*UPO-II (PDB code: 9HE6). Our refined model became the template for the rest of the datasets. For automated rigid body refinement, REFMAC within the CCP4 suite [28] was used and 5% of structure factor amplitudes were randomly selected in the calculation of free R-factor. Then, Coot [29] was used for manual refinement and model building of the ligands and at the later steps, glycans and water molecules were added, which, combined with more rounds of restrained refinement, led to final statistics reported in **Supplementary Table S1**.

For the complexed structures, substrates were solved in 99% (*v*/*v*) methanol. Preformed Grogu crystals were soaked in the precipitant solution, supplemented with 20–60 mM ligand for one to

21 h. Since most of the soaking experiments were unsuccessful, cocrystallization was rehearsed with the corresponding ligands at concentrations from 28 to 58 mM and incubation times from 30 to 60 min. As before, the obtained crystals were cryoprotected with 25% (*v*/*v*) glycerol and diffraction data collected at ALBA synchrotron were processed with XDSGUI and AIMLESS programs. The complexes were solved by Fourier synthesis using the coordinates from the unsubstituted form and substrate ligands, solvent molecules and waters were manually fitted into the density with Coot. Details for complexes with tetradecane, lauric acid, α-ionone, and α-damascone are provided in **Supplementary Table S1**.

Verification of these structures was done via PDB validation server (validate.wwpdb.org) before coordinates and associated structure factors were deposited in PDB. The structural figures were prepared with PyMOL.

Accession codes: Atomic coordinates and structure factors of Grogu and its complexes have been deposited in the Protein Data Bank (PDB), under the following IDs: 9RFY (protein), 9RFZ (tetradecane), 9RG0 (lauric acid), 9RG2 (α-damascone) and 9RG1 (α-ionone).

Enzymatic reactions: Experimental conditions were based on previously reported experiments with *Pab*UPO-II and specific details for each experiment are provided in the corresponding figure captions of this article [17].

GC/MS analyses: All the reactions products were recovered by liquid–liquid extraction with *tert*-butyl ether (for alkanes and fatty acids), or ethyl acetate (for α-damascone and α-ionone). Afterward, samples were dried under N_2 atmosphere, resuspended in 100 µL of pyridine (anhydrous) and derivatized with 100 µL of BSTFA, for 30 min at 70°C. GC/MS analyses were performed using a Shimadzu QP2020 system and a SH-Rxi-5 MS fused-silica capillary column (30 m x 0.25 mm i.d., 0.25 µm film thickness) (Shimadzu Japan). The oven program started at 50°C (held 1.5 min), ramped to 90°C at 30°C min^{-1} (held 2 min), and then to 250°C at 8°C min^{-1} (held 15 min). Derivatized and filtered samples (1 µL) were injected with a split ratio of 1:10 at 250°C, while the transfer line was maintained at 300°C. Product identification relied on mass fragment analysis, comparison with the reference spectra found in Wiley and NIST libraries, and published mass spectra data for each compound (**Supplementary Figure S3**).

4.1 | Molecular Dynamics Simulations

System setup: Initial coordinates for system set up were taken from the crystal structure of Grogu. The protonation state of titratable residues was determined at pH equivalent to 7 using the semiempirical program PropKa ver. 3.0.3 [30]. After the pKa analysis, Asp89 was assigned to be protonated, His22, His54, His86, and His255 were determined to be protonated at position *N*-ε, and the rest of His residues were assigned to be protonated at *N*-δ AMBER parameters for the oxoferryl Compound I (Cpd I), and the Cys40 involved in the Fe coordination was taken from the data published by Cheatham and coworkers [31]. Protein and water parameters were described using the AMBER ff14 SB [32] and TIP3P [33] force fields, respectively. Missing hydrogen atoms were added to the system according to their protonation state. Each system was solvated in a $82 \times 76 \times 78$ $Å^3$ orthorhombic box of waters (padding of 10 Å from protein surface). To neutralize the total negative charge, Na^+ counterions were added to the system. System preparation was carried out using tLEAP as part of AmberTools25 package [34, 35].

MD simulations: The MD simulations were performed on system using OpenMM v.8.2.0 as engine [36]. Nonbonding interactions were computed using the particle mesh Ewald with a cutoff for short-range interactions of 10 Å. All simulations were run under NPT conditions. Temperature was maintained at 303.15 K using a Langevin thermostat, and pressure controlled at 1 atm using a Montercalo barostat. We used an integration step of 2 fs. Initial energy minimization was done to relax the starting geometry, followed by a gradual heating up, increasing the temperature by 1 K every picosecond until reaching final 303.15 K. This was followed by a 0.5 ns equilibration run. Finally, a last NPT production run of 500 ns was carried out. To improve sampling, four replicas were collected making a total of 1.5 µs.

MD trajectory analysis: Channel geometry along the trajectory was characterized by tracing the centerline from the Cpd I Fe^{4+} to the channel exit, defined as the centroid enclosed by the Cα atoms of the most distal residues lining the channel. The centerline was constructed on a predefined voxelized grid and reconstructed as a monotonically increasing path along the *z*-axis that connects the Cpd I Fe^{4+} to the exit centroid. The local channel radius along the centerline was computed as the minimum distance to any protein heavy atom. Shape descriptors, including tortuosity, bottleneck radius, channel volume, and Jaccard distance, were evaluated along the trajectory. In addition, the conformation of Met73 was mapped throughout the trajectory and classified according to its similarity to the alternate A and B conformations observed in the crystal structures. This classification was performed using both RMSD and χ dihedral angles relative to the crystallographic references. Finally, trajectories were partitioned based on Met73 conformational states A and B, and a principal component analysis (PCA) of the channel descriptors was done on each partition. Representative centerlines and protein structure frames corresponding to the maxima of the PCA projections were extracted for structural inspection and subsequent docking studies. All analyses were performed in Python v3.12 using MDTraj v1.11.0, SciPy v1.15.2, and NumPy v2.2.6.

Docking studies of α-damascone and α-ionone: Ligand conformers were generated using RDKit v2024.03.6 [37] from their SMILES strings, with geometry optimization. Docking calculations were performed using AutoDock Vina v1.2.7 [38] for each ligand against the three states extracted from channel shape. Gasteiger charges (which are used in AutoDock) of Cpd I were computed using RDKit. The search space was defined by a cubic box of $20 \times 20 \times 20$ $Å^3$ centered on the oxoferryl oxygen of Cpd I. Docking parameters were set to an exhaustiveness of 16, an energy range of 10 kcal·mol^{-1}, a minimum RMSD between poses of 1.0 Å, and a maximum number of poses of 20. A final relaxation step was done implemented in OpenMM. Binding energies were computed in terms of MM/GBSA as implemented in AmberTools.

Acknowledgments

This work was supported by the I+D+I PID2022-142074OB-I00-RAINBOW, PID2022-136367OB-C33, and PID2019-106166RB-I00-OXYWAVE, Spanish projects funded by MCIN/AEI/10.13039/

501100011033/FEDER, UE. Patricia Gomez de Santos thanks the Ministry of Science and Innovation for her Torres Quevedo contract as part of the PTQ2020-011037 project funded by MCIN/AEI/10.13039/501100011033 within the NextGenerationEU/PRTR. We thank the Synchrotron Radiation Source at ALBA (Barcelona, Spain) for assistance with the BL13-XALOC beamline.

Conflicts of Interest

The authors declare no conflicts of interest.

Data Availability Statement

Research data are not shared.

References

1. M. Hofrichter, H. Kellner, R. Herzog, et al., *Fungal Peroxygenases: A Phylogenetically Old Superfamily of Heme Enzymes with Promiscuity for Oxygen Transfer Reactions", in Grand Challenges in Fungal Biotechnology, Grand Challenges in Biology and Biotechnology* (Cham: H. Nevalainen (Springer, 2020). 369–403.

2. A. Beltrán-Nogal, I. Sánchez-Moreno, D. Méndez-Sánchez, P. Gómez de Santos, F. Hollmann, and M. Alcalde, "Surfing the Wave of Oxyfunctionalization Chemistry by Engineering Fungal Unspecific Peroxygenases," *Current Opinion in Structural Biology*, 73 (2022): 102342.

3. D. T. Monterrey, A. Menés-Rubio, M. Keser, D. Gonzalez-Perez, and M. Alcalde, "Unspecific Peroxygenases: The Pot of Gold at the End of the Oxyfunctionalization Rainbow?," *Current Opinion in Green and Sustainable Chemistry*, 41 (2023): 100786.

4. X. Xu, Y. Mao, M. Martinez, et al., "Peroxygenase-Catalysed Selective Oxidation of Silanes to Silanols," *Angewandte Chemie International Edition*. (2023): e202302844.

5. A. Swoboda, Z. Duhović, I. E. E. Kroschel, et al., "Stereocomplementary Unspecific Peroxygenases for Asymmetric Anti-Markovnikov Wacker-Type Oxidation and Epoxidation of Styrenes," *ACS Catalysis*, 17 (2024): 13334–13342.

6. J. Li, K. A. S. Cornish, B. Pogrányi, et al., "Cyclopropanation Reactions by a Class I Unspecific Peroxygenase," *Organic and Biomolecular Chemistry*, 20 (2025): 4897–4901.

7. D. Homann, L. Thomas-Hargreaves, and P. Püllmann, "Probing Unspecific Peroxygenases for Non-Natural Nitrene Chemistry," *Chembiochem: A European Journal of Chemical Biology*, 16 (2025): e202500332.

8. M. Zámocký, B. Kubala, B. Zámocká, J. Kronek, and F. Hollmann, "Molecular Diversity of Unspecific Heme Peroxygenases with Promising Applications in Sustainable Oxyfunctionalizations," *International Journal of Macromolecules* 329 (2025): 147823.

9. K. Piontek, E. Strittmatter, R. Ullrich, et al., "Structural Basis of Substrate Conversion in a New Aromatic Peroxygenase: Cytochrome P450 Functionality with Benefits," *Journal of Biological Chemistry*, 48 (2013): 34767–34776.

10. M. Ramirez-Escudero, P. Molina-Espeja, P. Gomez de Santos, M. Hofrichter, J. Sanz-Aparicio, and M. Alcalde, "Structural Insights into the Substrate Promiscuity of a Laboratory-Evolved Peroxygenase," *ACS Chemical Biology*, 12 (2018): 3259–3268.

11. X. Fu, K. Lin, X. Zhang, Z. Guo, L. Kang, and A. Li, "Identification, Heterologous Expression and Characterization of a New Unspecific Peroxygenase from, *Marasmius Fiardii*, PR-910," *Bioresources and Bioprocessing* 11 (2024): 33.

12. I. Sánchez-Moreno, A. Fernandez-Garcia, I. Mateljak, et al., "Structural Insights and Reaction Profile of a New Unspecific Peroxygenase from, *Marasmius Wettsteinii*, Produced in a Tandem-Yeast Expression System," *ACS Chemical Biology*, 10 (2024): 2240–2253.

13. R. Ullrich, J. Nüske, K. Scheibner, J. Spantzel, and M. M.Hofrichter, "Novel Haloperoxidase from the Agaric Basidiomycete *Agrocybe Aegerita* Oxidizes Aryl Alcohols and Aldehydes," *Applied and Environmental Microbiology*, 8 (2004): 4575–4581.

14. P. Molina-Espeja, E. Garcia-Ruiz, D. Gonzalez-Perez, R. Ullrich, M. Hofrichter, and M. Alcalde, "Directed Evolution of Unspecific Peroxygenase from *Agrocybe Aegerita*," *Applied and Environmental Microbiology*, 11 (2014): 3496–3507.

15. D. Deng, Z. Jiang, L. Kang, et al., "An Efficient Catalytic Route in Haem Peroxygenases Mediated by O_2/Small-Molecule Reductant Pairs for Sustainable Applications," *Nature Catalysis*, 1 (2025): 20–32.

16. P. Gomez de Santos, M. Dat Hoang, J. Kiebist, et al., "Functional Expression of Two Unusual Acidic Peroxygenases from *Candolleomyces Aberdarensis* in Yeasts by Adopting Evolved Secretion Mutations," *Applied and Environmental Microbiology*, 19 (2021): e0087821.

17. A. Menés-Rubio, A. Fernandez-Garcia, D. T. Monterrey, et al., "Characterization of Recombinant Unspecific Peroxygenase from *Candolleomyces Aberdarensis* through Crystallographic and Substrate Selectivity Studies," *ChemCatChem*, 7 (2025): e202402015.

18. PDBePISA server,, https://www.ebi.ac.uk/pdbe/pisa/.

19. M. Hofrichter, H. Kellner, M. J. Pecyna, and R. Ullrich, *Fungal Unspecific Peroxygenases: Heme-Thiolate Proteins that Combine Peroxidase and Cytochrome P450 Properties", in Monooxygenase, Peroxidase and Peroxygenase Properties and Mechanisms of Cytochrome P450. Advances in Experimental Medicine and Biology*. In: E. Hrycay ed. and S. Bandiera (Springer, Cham, 2015, pp. 341–368, 851

20. E. D. Babot, J. C. del Río, L. Kalum, A. T. Martínez, and A. Gutiérrez, "Oxyfunctionalization of Aliphatic Compounds by a Recombinant Peroxygenase from *Coprinopsis Cinerea*," *Biotechnology and Bioengineering*, 9 (2013): 2323–2332.

21. ESPript 30 server, https://espript.ibcp.fr.

22. E. D. Babot, C. Aranda, J. C. del, and etal Río, "Selective Oxygenation of Ionones and Damascones by Fungal Peroxygenases," *Journal of Agriculture and Food Chemistry*, 19 (2020): 5375–5383.

23. P. Gomez de Santos, I. Mateljak, M. Dat Hoang, S. J. Fleishman, F. Hollmann, and M. Alcalde, "Repertoire of Computationally Designed Peroxygenases for Enantiodivergent C–H Oxyfunctionalization Reactions," *Journal of American Chemical Society*, 6 (2023): 3443–3453.

24. A. Beltran-Nogal, I. Mateljak, D. Gonzalez-Perez, and M. Alcalde, "Engineering Unspecific Peroxygenases by Structure-Guided In Vivo Recombination of Homologous Protein Blocks," *Methods in Enzymology: Biocatalysis*, 714 (2025): 407–423.

25. W. Kabsch, "Xds," *Acta Crystallographica Section D: Biological Crystallography*, 2 (2010): 125–132.

26. P. R. Evans and G. N. Murshudov, "How Good Are My Data and What Is the Resolution?," *Acta Crystallographica Section D: Biological Crystallography*, 7 (2013): 1204–1214.

27. A. Vagin and A. Teplyakov, "Molecular Replacement with MOLREP," *Acta Crystallographica Section D: Biological Crystallography*, 1 (2010): 22–25.

28. G. N. Murshudov, A. Vagin, A. Lebedev, K. S. Wilson, and E. J. Dodson, "REFMAC5 for the Refinement of Macromolecular Crystal Structures," *Acta Crystallographica Section D: Biological Crystallography*, 4 (2011): 355–367.

29. P. Emsley, B. Lohkamp, W. G. Scott, and K. Cowtan, "Features and Development of Coot," *Acta Crystallographica Section D: Biological Crystallography*, 4 (2010): 486–501.

30. M. H. M. Olsson, C. R. Søndergaard, M. Rostkowski, and J. H. Jensen, "PROPKA3: Consistent Treatment of Internal and Surface Residues in

Empirical pKa Predictions," *Journal of Chemical Theory and Computation*, 2 (2011): 525–537.

31. K. Shahrokh, A. Orendt, G. S. Yost, and T. E. Cheatham, "Quantum Mechanically Derived AMBER-Compatible Heme Parameters for Various States of the Cytochrome P450 Catalytic Cycle," *Journal of Computational Chemistry*, 2 (2012): 119–133.

32. J. A. Maier, C. Martinez, K. Kasavajhala, L. Wickstrom, K. E. Hauser, and C. Simmerling, "ff14SB: Improving the Accuracy of Protein Side Chain and Backbone Parameters from ff99SB," *Journal of Chemical Theory and Computation*, 8 (2015): 3696–3713.

33. W. L. Jorgensen, J. Chandrasekhar, J. D. Madura, R. W. Impey, and M. L. Klein, "Comparison of Simple Potential Functions for Simulating Liquid Water," *Journal of Chemical Physics*, 2 (1983): 926–935.

34. D. A. Case, H. M. Aktulga, K. Belfon, et al., *AMBER*. San Francisco: University of California, 2025, 2025

35. D. A. Case, H. M. Aktulga, K. Belfon, et al., "AmberTools," *Journal of Chemical Information and Modeling*, 20 (2023): 6183–6191.

36. P. Eastman, R. Galvelis, R. P. Peláez, et al., "OpenMM. 8: Molecular Dynamics Simulation with Machine Learning Potentials," *Journal of Physical Chemistry B*, 1 (2024): 109–116.

37. G. Landrum, P. Tosco, B. Kelley, et al., *Rdkit/Rdkit:2024_03_6 (Q1 2024) Release* (Zenodo 2024).

38. O. Trott and A. J. Olson, "AutoDock Vina: Improving the Speed and Accuracy of Docking with a New Scoring Function, Efficient Optimization, and Multithreading," *Journal of Computational Chemistry* 31, no. 2 (2010): 455–461.

Supporting Information

Additional SI can be found online in the Supporting Information section.